analytical chemistry

pubs.acs.org/ac Article

Complementary Metal–Oxide–Semiconductor Potentiometric Field-Effect Transistor Array Platform Using Sensor Learning for Multi-ion Imaging

Nicolas Moser,[§] Chi Leng Leong,[§] Yuanqi Hu, Chiara Cicatiello, Sally Gowers, Martyn Boutelle,* and Pantelis Georgiou*

Cite This: *Anal. Chem.* 2020, 92, 5276–5285

Read Online

ACCESS | Metrics & More | Article Recommendations | Supporting Information

ABSTRACT: This work describes an array of 1024 ion-sensitive field-effect transistors (ISFETs) using sensor-learning techniques to perform multi-ion imaging for concurrent detection of potassium, sodium, calcium, and hydrogen. Analyte-specific ionophore membranes are deposited on the surface of the ISFET array chip, yielding pixels with quasi-Nernstian sensitivity to K^+, Na^+, or Ca^{2+}. Uncoated pixels display pH sensitivity from the standard Si_3N_4 passivation layer. The platform is then trained by inducing a change in single-ion concentration and measuring the responses of all pixels. Sensor learning relies on offline training algorithms including *k*-means clustering and density-based spatial clustering of applications with noise to yield membrane mapping and sensitivity of each pixel to target electrolytes. We demonstrate multi-ion imaging with an average error of 3.7% (K^+), 4.6% (Na^+), and 1.8% (pH) for each ion, respectively, while Ca^{2+} incurs a larger error of 24.2% and hence is included to demonstrate versatility. We validate the platform with a brain dialysate fluid sample and demonstrate reading by comparing with a gold-standard spectrometry technique.

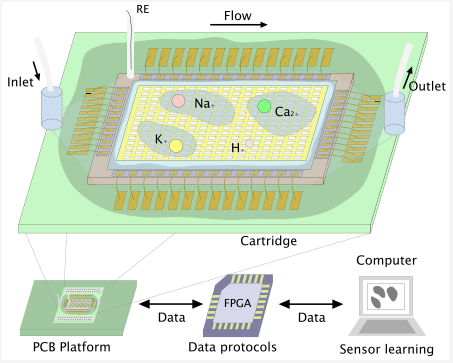

Over the past decade, technological advances in the field of sensors have allowed the development of new medical devices to monitor human health by targeting various biomarkers and to take a step closer to automated medicine. Due to their essential role in proper operation of the body, ions are ideal targets, as electrolyte imbalance may appear as a first sign of severe health issues, including renal failure,[1] nausea, malaise, and collapse,[2] where early detection could allow preventive treatment.

This research focuses on the detection of secondary damage after traumatic brain injury (TBI). In the case of TBI, primary injuries occur irreversibly following the impact and damaging the blood vessels, axons, nerve cells, and glia of the brain. Such damage can also initiate a cascade of events resulting in delayed secondary injuries. Spreading depolarizations (SD) are seen frequently in injured cerebral tissue[3−5] and are thought to be a possible mechanism by which secondary injuries develop.[6] Approximately 40% of TBI patients deteriorate in the days after the initial injury,[7] due to the onset of secondary injury, during which the patients are being monitored in the intensive care unit. SD represent a better indicator of the occurrence of secondary injuries than any of the factors currently used and predict poor patient outcome.[8] First described by Leao,[9] SD represents a wave of almost total depolarization of neurones and gills cells moving slowly across the cortex. This leads to a temporary breakdown in ion homeostasis and a disruption of cortical function. In the human brain we have shown SD to lead to a rise in brain potassium[10] and to have profound effects on the availability of brain glucose.[10,11] As such, measuring ion concentration in brain fluid allows one to detect SD in an attempt to allow clinicians to intervene early in saving ischemic but potentially viable cerebral tissue.

Several attempts have been made to achieve multi-ion sensing using optical sensing methods. While the earliest reports involved tagging ions with fluorescent dyes,[12,13] integration of the sensing element within a common substrate was achieved using ion-sensing capillaries and optode membranes, relying on external components including a light source and a charged–coupled device (CCD) camera.[14] In this structure, ion selectivity relies on the use of an ionophore inside the capillary or the membrane, acting as a transducer to the optode.[15] Despite attempts to develop optical setups, chemical sensing has appeared as the most successful approach so far for multi-ion imaging, coating sensors with polymeric ion-selective membranes to provide specificity to a broad range of ionic species. Yoshinobu et al.[16] have leveraged the optical

Received: December 27, 2019
Accepted: March 6, 2020
Published: March 6, 2020

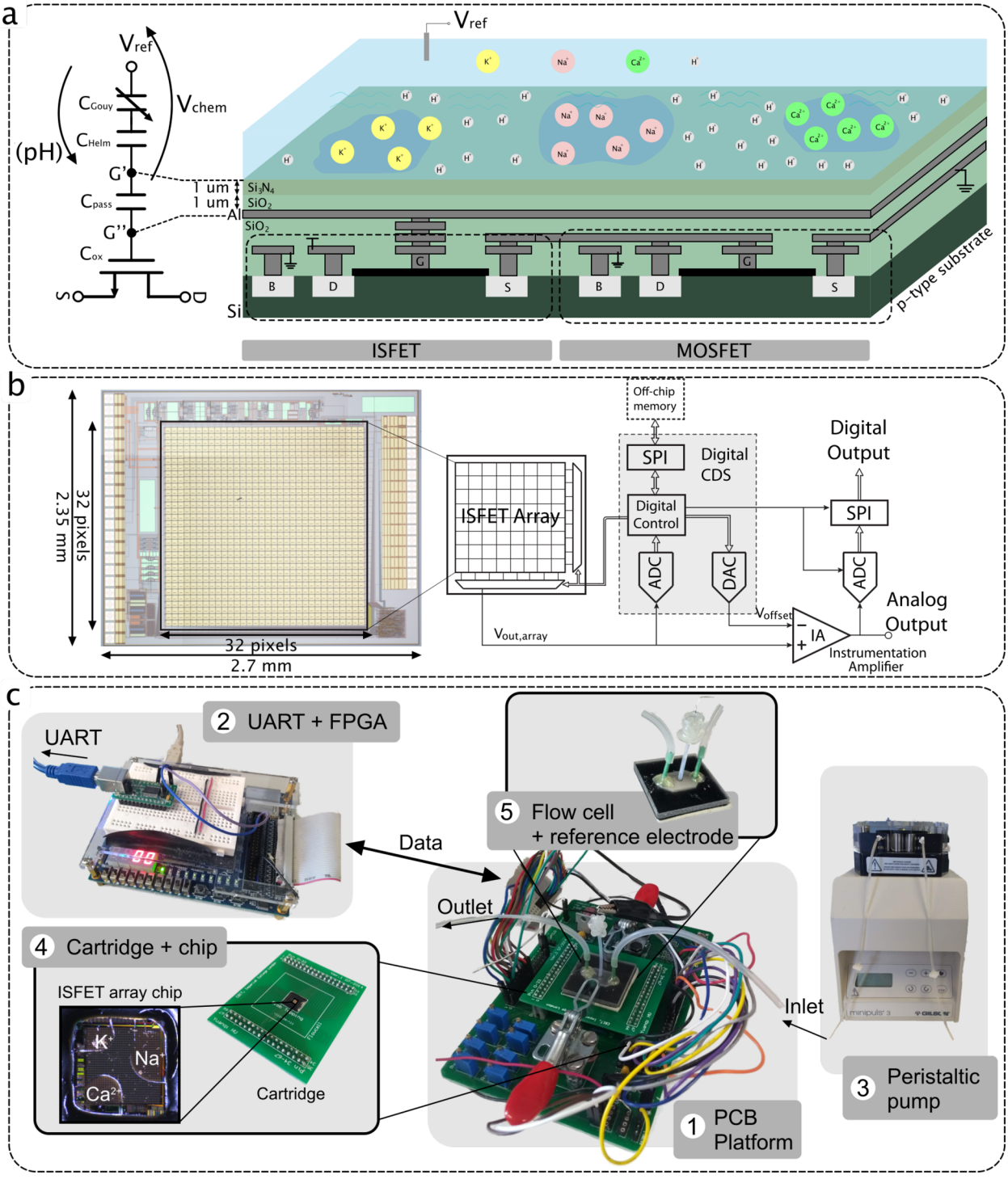

Figure 1. (a) Cross-section diagram of the ISFET structure in unmodified CMOS technology emphasizing that both an ISFET sensor and a MOSFET can be incorporated on the same substrate (left) and an equivalent ISFET macromodel (right).[40] (b) System architecture (right) and a microphotograph (left) of the ISFET array fabricated in AMS 0.35 μm.[30] (c) Experimental setup for ion sensing including (1) the main PCB platform, (2) the FPGA, (3) the peristaltic pump, (4) the microchip mounted on a cartridge, and (5) the flow cell.

properties of semiconductor technology to introduce the light-addressable potentiometric sensor (LAPS) for multi-ion sensing, demonstrating imaging by placing stripes of K^+- and Ca^{2+}-selective membranes. The approach was further pushed to improve on frame rate and include microfluidic capabilities,[17,18] but it still suffers from limitations in terms of portability due to the requirement of external components. Complementary metal−oxide−semiconductor (CMOS) technology has appeared as a solution for designing system-on-chips (SoCs) on silicon integrated robustly with thousands of sensors, at low power and low cost. CMOS sensors have demonstrated their potential with optical imagers, which have grown significantly following their implementation in CMOS technology, integrating millions of active pixel sensors on large-scale arrays.[19−21] More recent work includes the development of CMOS electrode arrays to perform intracellular recordings

https://dx.doi.org/10.1021/acs.analchem.9b05836
Anal. Chem. 2020, 92, 5276−5285

from thousands of neurons in vitro[22] or electrochemical monitoring of tissues ex vivo,[23] highlighting the versatility of and opportunities for CMOS technology in integrated sensors. Building on such advances, Hattori et al.[24,25] have developed a 16K array of chemical CCD sensors and demonstrated the platform for potassium and sodium imaging. The sensors provide ion sensitivity by varying output potential on the basis of a charge transfer technique; however, they are fabricated in a modified CMOS process with controlled surface deposition and etching steps,[26] and they have not been demonstrated in concurrent monitoring of several ionic species.

This work relies on the ion-sensitive field-effect transistor (ISFET)[27,28] as a solid-state sensor compatible with unmodified CMOS technology,[29] removing the need for a special fabrication process while providing benefits for scalability, robustness, low cost, and monolithic integration with bespoke instrumentation. The principle of detection relies on the modulation of the FET threshold voltage by the electric field generated when ionic species in solution bind to the surface of the chip. Electrolyte specificity is provided by the sensing layer, and so far we have extensively demonstrated ISFET operation toward H^+ sensing, taking advantage of the inherent pH sensitivity of the Si_3N_4 passivation layer in unmodified CMOS technology.[29−32] This has enabled DNA sequencing with the Ion Torrent platform,[33] which has been a revolution in terms of cost and high throughput, but also other applications such as cellular imaging[32] or DNA detection.[31,34] The compatibility of ISFETs with ion-sensitive membranes was validated for individual sensors,[35,36] and we have previously reported a proof-of-concept study demonstrating potassium and sodium sensitivity.[37]

We present an ISFET array-based multi-ion imaging platform for concurrent monitoring of pH, potassium, sodium, and calcium. The versatility of the approach toward detection of multiple ionic species using ion-sensitive membranes requires specific algorithms to train the array, discriminate species, and provide measurements of ionic concentrations. We introduce the concept of sensor learning for ISFET arrays, relying on back-end offline training algorithms to process data from calibration runs and to generate a sensitivity matrix to enable accurate monitoring capabilities through ion imaging. The approach combines for the first time (1) integrated sensors in unmodified CMOS technology, i.e., which do not require additional postprocessing techniques, (2) versatile sensing on an array exposed to the ion-sensitive membranes to target a panel of four ions, (3) compensation mechanisms for temporal drift, (4) sensor-learning mechanisms for offline training of the array using a model based on the ionic strength of the solution and a clustering algorithm, and (5) an estimate of concentration change in all targeted species. Due to the flexibility of the approach, the device can be considered for a wide range of applications for monitoring and diagnostics. The technology is demonstrated in this work for the detection of secondary damage after TBI.

EXPERIMENTAL SECTION

The ISFET. The ISFET is a solid-state sensor with a structure relying on a floating gate metal−oxide−semiconductor field-effect transistor (MOSFET) where the gate is covered with an insulating membrane and the device is biased through an external reference electrode exposed to the solution.[27,28] Much research has been dedicated to fabricating custom ISFET structures with improved characteristics such as a dual gate[38] or alternative sensing layers.[39] However, the device can also be implemented in standard CMOS technology using the extended-gate approach,[29] which consists of extending the ISFET gate to the top metal through a stack of vias, as shown in Figure 1a. The sensing surface of the device is then considered the top metal area that is in contact with the solution through the passivation layer of the CMOS process.

The device operation relies on a logarithmic shift of the threshold voltage with any variation in ion concentration. In particular, the threshold voltage is shown to be dependent on the potential due to the reference electrode (E_{ref}), the potential due to the existence of dipole molecules in the solution (χ_{sol}), the work function of the metal contact (ϕ_m), and the chemical potential related to ion concentration (ψ_0), following the relationship[40]

$$V_{th(ISFET)} = E_{ref} - \psi_0 + \chi_{sol} - \frac{\phi_m}{q} + V_{th(MOSFET)} \quad (1)$$

The chemical related terms can be grouped as a potential (V_{chem}) written as

$$V_{chem} = E_{ref} - \psi_0 + \chi_{sol} - \frac{\phi_m}{q} \quad (2)$$

In eq 2, the sensitivity to ionic species is reflected in ψ_0, which is governed by two chemical phenomena: the site binding of the insulator and the capacitive double layer. The site-binding model[41] dictates the way that ions in solutions bind to discrete surface sites on the Si_3N_4 layer. Similarly, due to the presence of ions in solution, a double-layer capacitor is formed at the surface of the sensor from a Helmholz plane and a Gouy−Chapman layer.[42] Overall, V_{chem} can be expressed in terms of the concentration x_i or the activity a_i of the ion i present in solution[43]

$$V_{chem} = \Gamma - \alpha S_N \log(x_i) = \Gamma' - \alpha S_N \log(a_i) \quad (3)$$

where the activity is related to the concentration through the activity coefficient γ_i following $a_i = \gamma_i x_i$, $\Gamma = \Gamma' - \alpha S_N \log(\gamma_i)$ groups all nonionic related terms, and α reflects the deviation from the Nernstian sensitivity $S_N = (2.3RT)/F \approx 59$ mV at ambient temperature. (Note that Γ is equivalent to γ in our previous publications but has been redefined here for clarity.)

In this paper, the solutions cannot be considered ideal and we will express the model in terms of the activity of all species. We quantify the ionic strength I of each solution as

$$I = \frac{1}{2}\sum_{i=1}^{N} x_i z_i^2 \quad (4)$$

where z_i is the charge of ion i. The activity coefficient γ_i is then computed for each ion i following Davies equation

$$\log(\gamma_i) = -Az_i^2\left(\frac{\sqrt{I}}{1+\sqrt{I}} - 0.3I\right) \quad (5)$$

where A is a constant related to factors such as temperature and the permittivity of the media. For liquids, we can approximate $A \approx 0.51\ M^{-1/2}$.

Figure 1a also shows the behavioral macromodel of the ISFET, biased by the reference electrode voltage V_{ref} and including the chemical voltage V_{chem}. The effective gate voltage $V_{g's}$ is expressed as

https://dx.doi.org/10.1021/acs.analchem.9b05836
Anal. Chem. 2020, 92, 5276−5285

$$V_{g's} = V_{gs} - V_{chem} \quad (6)$$

The passivation layer of the considered CMOS technology (AMS 0.35 μm), made from Si_3N_4 and SiO_2, can be modeled as an extra capacitance C_{pass} called passivation capacitance. The value of C_{pass} can be approximated using the equation

$$C_{pass} \approx (WL)_{chem}\varepsilon_0 \frac{\varepsilon_{Si_3N_4}\varepsilon_{SiO_2}}{\varepsilon_{Si_3N_4}t_{SiO_2} + \varepsilon_{SiO_2}t_{Si_3N_4}} \quad (7)$$

where ε_0 is the permittivity of vacuum, ε_x is the permittivity of layer x, t_x is the thickness of layer x, and $(WL)_{chem}$ is the sensing surface. In the model, C_{pass} causes signal attenuation between the floating gate voltage $V_{g''}$ and the surface voltage $V_{g'}$ due to capacitive division with the series capacitances C_{ox} and C_d of the transistor.[40] The division is written as

$$V_{g''} = \frac{C_{pass}}{C_{pass} + (C_{ox}C_d)/(C_{ox} + C_d)} \times V_{g'} \quad (8)$$

The ISFET suffers from several nonidealities. Due to the floating nature of the transistor gate, trapped charge creates a shift in the $I-V$ curve of the device, modeled as an extra offset voltage V_{tc} in the model of Figure 1a. Surface chemistry also induces a slow temporal drift in the output response of the sensor.[40] This sets several challenges to the design and special methods are required to cancel pixel mismatch.

On-Chip ISFET Array. In this work, we use an ion-imaging array fabricated in AMS 0.35 μm CMOS technology and previously demonstrated for pH detection.[30,44] The 2.7 × 2.35 mm microchip integrates a 32 × 32 ISFET array, and its schematic architecture is shown in Figure 1b. Each pixel contains an ISFET-based analog-sensing front-end that amplifies the chemical signal on the basis of a capacitance ratio. A low-leakage switch allows one to periodically reset nonideal DC offsets at the floating gate of the ISFET, including trapped charge and drift effects.[44] However, due to leakage at the gate of the ISFET, the readout still suffers from electrical drift, which would naturally be interpreted as a drift in chemical concentration during the measurement.

On a system level, a digital correlated double sampling (CDS) scheme senses the offset value for each pixel and subtracts it from the multiplexed output. An analog-to-digital converter (ADC) then digitizes the analog output and sends it externally.

Experimental Setup. The experimental setup is shown in Figure 1c. Packaging of the CMOS chip within a wet environment is performed in three steps. (1) We glue the chip on a printed circuit board (PCB) cartridge with a conductive ground plane using silver-loaded epoxy, cured for 30 min at 120 °C. (2) We apply the electrical connections between the chip and the cartridge with a wedge wirebonder in cleanroom settings. (3) We cover the wirebonds with glob-top epoxy cured for 1 h at 100 °C. The cartridge is plugged on a board that integrates analog bias, power circuits, and digital interfacing to an external field programmable gate array (FPGA). The FPGA connects to MatLab through a UART protocol, allowing one to send and receive data.

All readings on the chip involving calibration standards are performed using a flow cell and a peristaltic pump (GILSON MINIPULS 3) to provide flow over the sensors. The flow cell has been fabricated using 3D printing combining an inlet and outlet, a hexagonal chamber, and a central hole to place the reference electrode. The bottom of the chamber is printed as a soft layer to act as a gasket when clamped on the board. Due to the limited volume for the brain dialysate fluid samples, readings were obtained by first injecting the fluid using a pipet, removing it, and injecting aCSF buffer solution. The order of operation was selected to avoid contaminating the sample for spectrometry.

The standard glass reference electrode cannot be used in this setting due to size requirements for the flow cell. Instead we have developed a disposable agar-based reference electrode as follows: (1) we chlorinate a 0.1 mm silver wire in 3 M KCl at a voltage of 1.3 V, (2) we fill a tube with boiling aCSF agar (aCSF solution with 5% agar concentration) to guarantee a fixed chloride concentration and a similar ionic strength to the test solution, and (3) we introduce the wire through the tube and wait for the gel to solidify.

The system operation then consists of (1) calibrating the array in a reference solution to set all pixels to baseline and (2) flowing the solution of interest to observe diffusion phenomena and measure variation in the concentration of the target ion(s).

Calibration Standards and Patient Sample. All calibration standard and solutions were made from HCl or the chloride salt NaCl, KCl, $CaCl_2$, and $MgCl_2$, in high-purity water (PURITE Select Fusion 40BP) following the concentrations indicated in Table 1. All chemicals were purchased from Sigma-Aldrich and of at least AnalaR grade. We consider artificial cerebrospinal fluid (aCSF) concentrations as the reference for all our measurements. Solutions with only one ion varying are then prepared for calibration. Lastly, solutions 1−3 (Sol 1−3) each provide a variation of two ionic species, and solution 4 (Sol 4) represents a logarithmic increase of 0.5 in the concentration of each species.

Table 1. Ion Concentrations (mM), pH, and Ionic Strength of Each Solution (mM)

identifier	KCl	NaCl	$CaCl_2$	$MgCl_2$	pH	I
aCSF solution	2.7	147	1.2	0.85	5.24	155.8
K^+ solution	27	147	1.2	0.85	5.65	180.1
Na^+ solution	2.7	14.7	1.2	0.85	5.33	23.5
Ca^{2+} solution	2.7	147	12	0.85	5.43	188.2
pH 4.3 solution	2.7	147	1.2	0.85	4.31	155.8
solution 1	2.7	50	5	0.85	5.37	10.3
solution 2	9	147	8	0.85	5.47	182.5
solution 3	20	100	1.2	0.85	5.51	126.2
solution 4	8.54	46.49	3.79	0.85	5.85	69
brain dialysate fluid	3.8	96.2	0.99	0.81	6.6	105.4

For TBI patient monitoring, a sterile clinical microdialysis catheter (CMA 70, 10 cm flexible shaft, 10 mm membrane length, 20 kDa cutoff; mDialysis, Stockholm, Sweden) was perfused with sterile physiological fluid (mDialysis), at 2 μL/min using a CMA 107 microinjection syringe pump (mDialysis). For clinical monitoring of TBI patients, written assent for study participation was obtained from legally authorized representatives, as patients were comatose at the time of inclusion. Written consent was obtained from patients themselves following this when possible. All human research procedures were approved by the King's College Hospital

https://dx.doi.org/10.1021/acs.analchem.9b05836
Anal. Chem. 2020, 92, 5276−5285

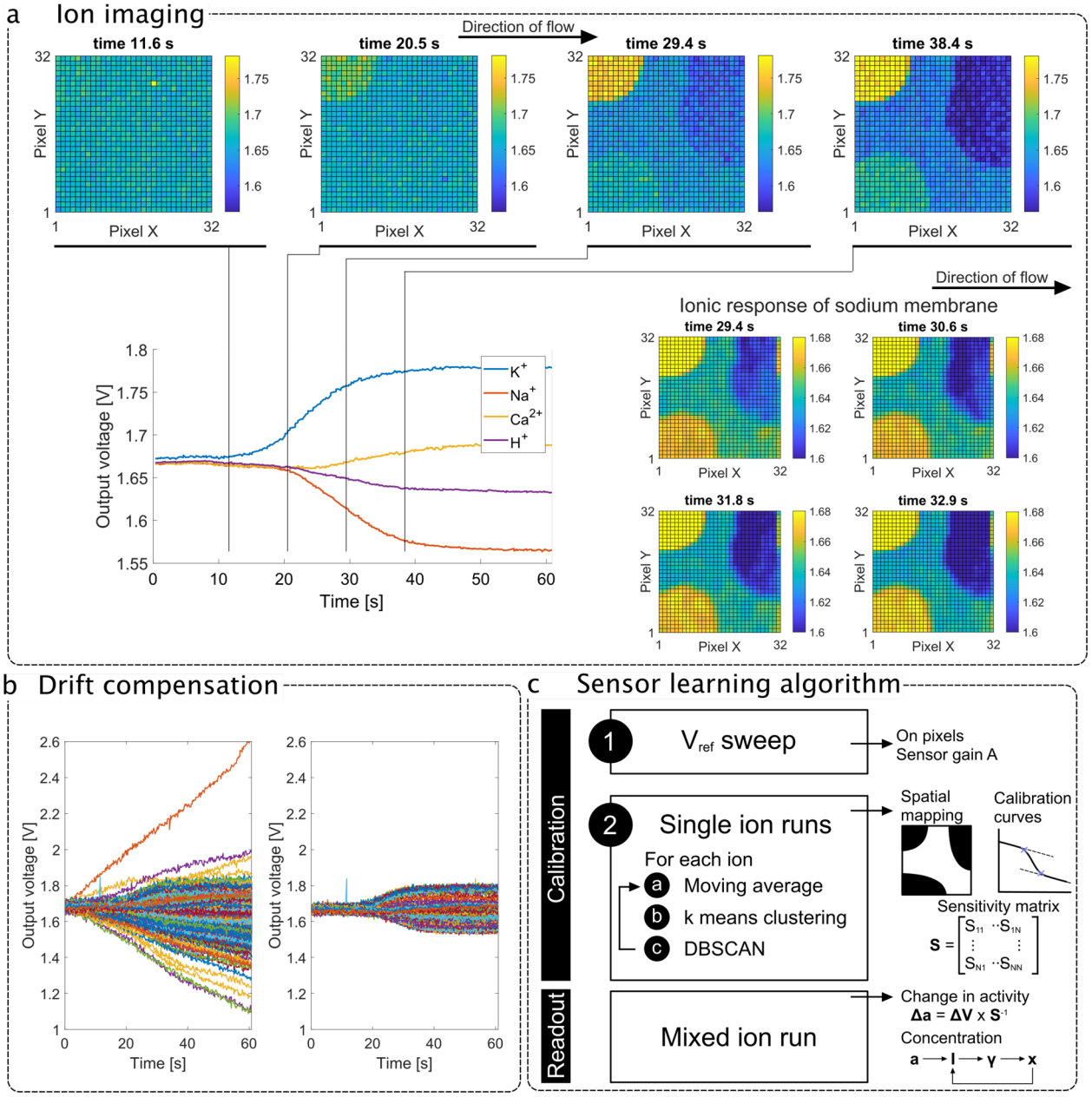

Figure 2. (a) Top: 2D visualization of four frames showing the sensor array output with potassium membrane responding first. Bottom left: Transient average compensated sensor output during an experiment where all ionic concentrations vary (from aCSF to Sol 4). Bottom right: 2D visualization of four frames showing the sensor array output, highlighting the ionic response of the sodium membrane with a narrower output range and demonstrating real-time ion-imaging capabilities of the ISFET array. The fluid flows from left to right. (b) Transient output for all sensors during an experiment where all ionic concentrations vary concurrently (from aCSF to Sol 4) before (left) and after (right) drift compensation. (c) The methodology for integrated sensor learning is first electrical (determination of gain through reference electrode voltage) and then chemical (single-ion run). An offline clustering-based algorithm identifies the sensing regions and their sensitivity. The measurement then involves estimating the activities and concentrations of each target electrolyte.

NHS Foundation Trust Ethical review board and were conducted in accordance with the Declaration of Helsinki.[10]

To validate the platform for brain dialysate fluid, inductively coupled plasma mass spectrometry (ICP-MS) was performed to determine an accurate concentration of metallic ions from the average of three runs. The pH of the solution was also measured using the pH probe. Table 1 includes the results.

Polymeric Ion-Selective Membranes. The ion-sensing membrane selectively binds with the ion of interest due to the presence of an ionophore. Although containing well-established components, the exact membrane recipe and fabrication methods were taught to us by Band,[45] an early pioneer in blood monitoring. The recipe for each membrane is as follows: (1) for potassium ion selective membrane, 5 mg of potassium ionophore (valynomycin), 164 mL of bis(2-ethylhexyl)sebacate, 2 mg of potassium tetrakis(4-chlorophenyl)borate, 66 mg of PVC, and 23.5 mL of tetrahydrofuran (THF); (2) for sodium ion selective membrane, 5 mg of sodium ionophore, 164 mL of bis(2-ethylhexyl)sebacate, 2 mg of potassium tetrakis(4-chlorophenyl)borate, 66 mg of PVC, and 23.5 mL of THF; and (3) for calcium ion selective membrane, 1 mg of calcium

https://dx.doi.org/10.1021/acs.analchem.9b05836
Anal. Chem. 2020, 92, 5276−5285

ionophore, 82 mL of bis(2-ethylhexyl)sebacate, 2 mg of potassium tetrakis(4-chlorophenyl)borate, 33 mg of PVC, and 22 mL of THF.

All the chemicals are obtained from Sigma-Aldrich (UK). The membranes are stored at 4 °C when not in use.

The membranes are characterized prior to the experiments on the ISFET array with solid-contact ion-selective electrodes (ISEs). The experimental results are included in Figure S1 (Supporting Information, SI) and demonstrate quasi-Nernstian sensitivities of 57.78 mV/dec (potassium), 56.44 mV/dec (sodium), and 25.79 mV/dec (calcium).

The membranes are diluted into 1 mL of tetrahydrofuran (THF) and deposited by pipetting 0.2 μL directly onto the surface of the chip, such as to avoid covered areas from overlapping. Figure 1c shows the result of the deposition as seen under the microscope. The membranes are left drying for 24 h to form a stable polymeric layer attached to the Si_3N_4 passivation layer. The planar and uniform Si_3N_4 surface layer in unmodified CMOS technology offers a radical change compared to previous sensing structure with ion-selective membranes. In past technologies, the gate was covered with a thin (10 nm) Si_3N_4 or SiO_2 surface.[27] In our structure, the sensor gate is extended with a "wire" fabricated using standard CMOS technology and the surface layer is significantly thicker (2 μm). In consequence, the membrane adheres to the surface layer and the robustness of sensing chips coated with ion-selective membranes is improved. A photograph of the ISFET array coated with the ion-sensitive membranes is shown in Figure 1c.

Membranes on-chip are preconditioned for 3 h before the start of experiments to mitigate drift. As was studied in previous work,[46] one of the main challenges for the lifetime of the device originates from the existence of a water layer at the membrane/sensing surface interface, which degrades membrane adhesion. Alternative structures have been reported, including the use of a water-repellent PMMA/PDMA copolymer and a POT solid contact[47] and a PEDOTF-TFAB[48] film aiming to increase the hydrophobicity of the surface contact. However, in this work, we have found the microchip encapsulation to be the limiting factor for the device lifetime. Indeed, after a certain time of exposure to the solution, the glob-top epoxy starts to degrade and liquid penetrates underneath, getting in contact with electrical pads and leading to failure of the sensing device. This translates into a gradual increase in reference electrode current during experimentation and hence a large drift in the sensor response. Overall, device lifetime extends to 5 days of experimentation, which is demonstrated in Figure S2 (SI) by providing a potassium membrane response on day 1 and day 5 of experimentation.

ISFET-Based Multi-ion Imaging. The top part of Figure 2a shows four frames of the 2D sensor array image during rapid solution flow where there is a change in the concentration of the four ions of interest (aCSF to Sol 4 in Table 1). The full data is also included as a video in the Supporting Information. The results highlight the location of the multiple ion-selective membranes during the solution flow, showing the potassium membrane first due to the solution flow from left to right, providing a validation for multi-ion imaging. The bottom left-hand corner of Figure 2a shows the transient output curve averages over each sensing region with annotated time stamps. From these curves we can extract a voltage variation that can be converted into an estimated concentration change. This highlights the need for a sensor-learning algorithm reflecting the surface coating of the sensors. The bottom right-hand corner further illustrates the concept of ion imaging by focusing on the ion response of the sodium membrane and demonstrating a gradual output variation from left to right within the sensing region.

Figure 2b shows individual pixel outputs corrupted by sensor drift on the left-hand side and compensated outputs showing the underlying chemical change on the right-hand side. The large drift of over 1 mV/s (absolute value varying with the sensor) is not typical of ISFET arrays. In this case, it originates from the switch at the floating gate of the ISFET, which is used to cancel offset at the expense of creating a leakage path and allowing a linear charge or discharge of the floating gate voltage.[30] Therefore, the drift is referred to as "electrical". Due to its repeatability and linearity, it can be compensated for and a drift-free sensor readout is achieved by subtracting the real-time measurement with output sampled prior to the experiment. To provide a point of comparison, the same technology without electrical leakage yields an ISFET "chemical" drift of 0.1 mV/s before conditioning, which is at least 1 order of magnitude lower than the electrical contribution.[31] Therefore, in this work, assuming regular calibrations with aCSF in the case of long measurements, linear compensation is sufficient because electrical drift is much larger than chemical drift.

Sensor-Learning Algorithm for Membrane Calibration. The methodology for sensor learning and ion monitoring is illustrated in Figure 2c. Sensor learning refers to the derivation of a sensitivity matrix for each sensing region through an offline two-point calibration phase. The steps are as follows: (1) the reference electrode voltage is raised by 100 mV to identify the active pixels and extract the sensor gain, which is discussed in more detail in the Supporting Information (Figure S3), and (2) single-ion runs are performed on the chip to extract selectivity and sensitivity toward target species. Following calibration, the sensors are able to read variations in ionic concentration for mixed-ion runs.

The offline training algorithm consists of three steps (the output of each step is included in the Supporting Information): (1) spatial moving average, (2) *k*-means clustering, and (3) density-based spatial clustering of applications with noise (DBSCAN).

For spatial moving average, the three-neighbor moving average is first applied for spatial filtering of sensor noise and drift, where the output of each pixel is spatially filtered as a weighted sum of its neighbors to the third order and the result is a smooth image with better differentiation of output levels due to the deposition of membranes (see Figure S4, SI).

The *k*-means clustering technique is the core of the clustering methodology of this algorithm. We consider that the array output can be classified in three levels: (1) highly sensitive to the target ion, which is the membrane we are trying to identify; (2) low sensitivity to the target ion, which is usually the nonselective top passivation layer; and (3) no sensitivity to the target ion, typically the other membrane-covered pixels. With this assumption, we separate the array output in three levels and identify the cluster with the maximum mean (or minimum mean for decreasing concentration) as the membrane-covered pixels (see Figure S5, SI).

Due to mismatch on the CMOS chip, some pixels on the edge of the array sometimes exhibit a different behavior, such as increased drift. As a result, the *k*-means algorithm picks up pixel noise that is not part of the membrane area. We apply

https://dx.doi.org/10.1021/acs.analchem.9b05836
Anal. Chem. 2020, 92, 5276−5285

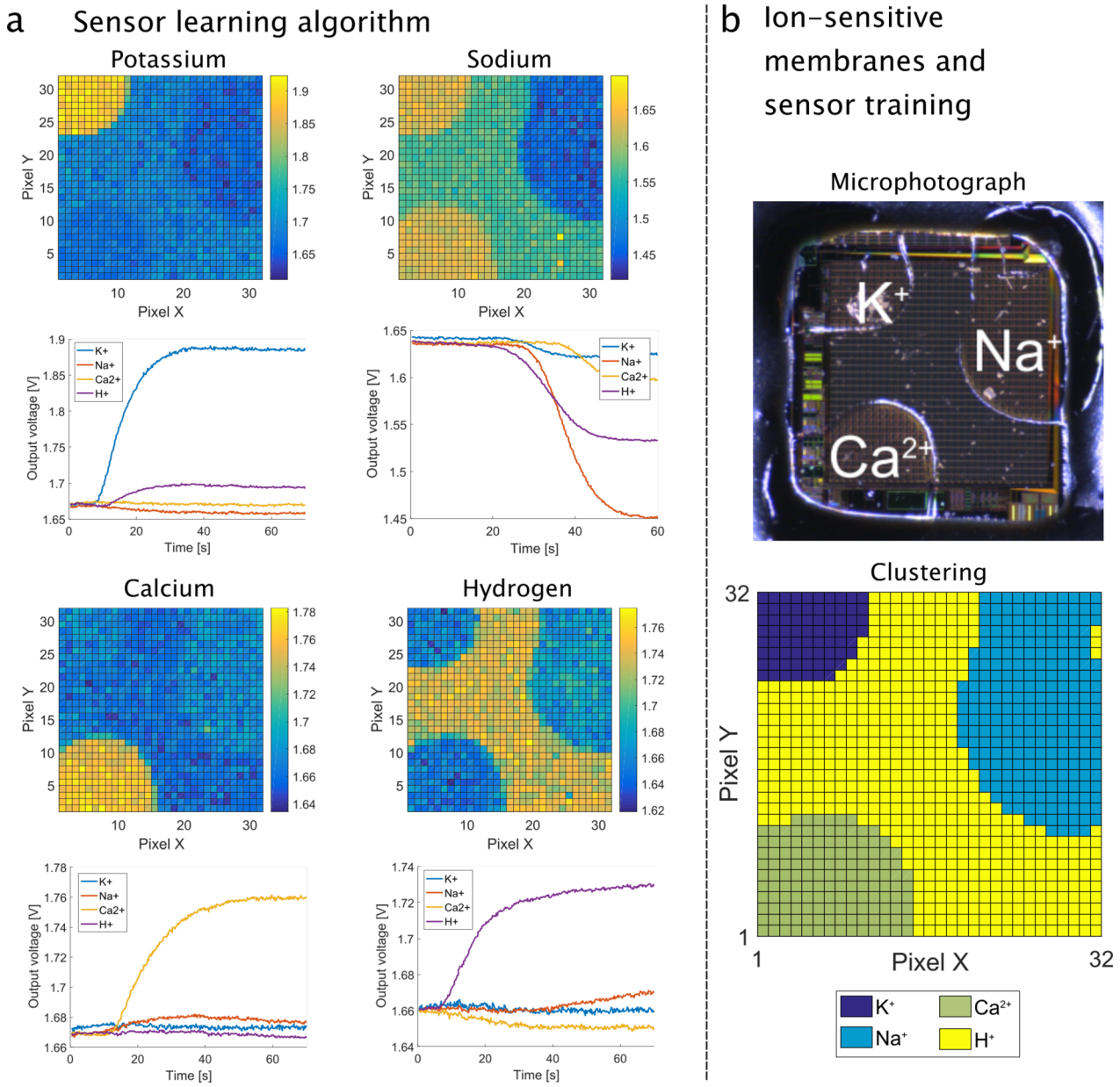

Figure 3. (a) The calibration of the sensors is performed by inducing a decade change in single-ion concentration (K^+, Na^+, Ca^{2+}, and H^+). For each ion, the top figure shows the 2D image of the array at the end of each run and the bottom figure shows the temporal output curves for each membrane as the solution is flowed in the chamber. (b) Top: Photograph of a chip under the microscope to show the location of each membrane. Bottom: Chip mapping as obtained after calibration by the clustering algorithm.

DBSCAN to classify the remaining cluster and identify the area with the highest number of pixels exposed (see Figure S6, SI).

The three steps are repeated for each single run to yield the chip mapping, i.e., a spatial representation of pixel selectivity to the ionic species. Once the pixels are classified, calibration curves for each membrane are obtained, including both chemical signal and linear sensor drift. In order to yield the sensitivity, we interpolate the drift linearly at the beginning and the end of the sample and consider the bounds of readout where the curve diverges from the interpolation as under 1 mV. From this calibration, the algorithm extracts the sensitivity matrix of the sensing platform.

Table 1 includes the ionic strength of each solution and highlights that its variation cannot be neglected when characterizing the sensitivity of the sensor. This is particularly true for the Na^+ solution due to the change in both Na^+ and Cl^- ions. As a result, the activity of each ion is computed as shown in eq 5 and the sensitivity matrix $\mathbf{S}$ such as $\mathbf{\Delta a} \times \mathbf{S} = \mathbf{\Delta V}$ is written as

$$\mathbf{S} = \begin{bmatrix} S_{K^+K^+} & S_{K^+Na^+} & S_{K^+Ca^{2+}} & S_{K^+H^+} \\ S_{Na^+K^+} & S_{Na^+Na^+} & S_{Na^+Ca^{2+}} & S_{Na^+H^+} \\ S_{Ca^{2+}K^+} & S_{Ca^{2+}Na^+} & S_{Ca^{2+}Ca^{2+}} & S_{Ca^{2+}H^+} \\ S_{H^+K^+} & S_{H^+Na^+} & S_{H^+Ca^{2+}} & S_{H^+H^+} \end{bmatrix} \quad (9)$$

where S_{xy} represents the sensitivity of membrane x to species y for a decade change in ionic activity.

Once the calibration is performed, the activity change in any solution of unknown ionic concentrations can be read as

https://dx.doi.org/10.1021/acs.analchem.9b05836
Anal. Chem. 2020, 92, 5276−5285

Table 2. Results for Ion Readings (mM) and pH with (w/) and without (w/o) the Novel Algorithm

			K^+	Na^+	Ca^{2+}	pH
Sol 1	concentration		2.7	50	5	5.37
	w/ algorithm	chip	2.68	54.3	2.99	5.36
		err. (%)	0.61	8.7	40	0.25
	w/o algorithm	chip	2.35	57.8	2.69	4.76
		err. (%)	13	16	46	11.4
Sol 2	concentration		9	147	8	5.47
	w/ algorithm	chip	8.58	148	6.4	5.47
		err. (%)	4.7	0.85	20	0.054
	w/o algorithm	chip	8.33	150	5.86	5.52
		err. (%)	7.5	1.9	27	0.97
Sol 3	concentration		20	100	1.2	5.51
	w/ algorithm	chip	18.8	96.4	1.23	5.36
		err. (%)	6.2	3.6	2.9	2.7
	w/o algorithm	chip	17.9	92.5	1.02	5.53
		err. (%)	11	7.5	15	0.35
Sol 4	concentration		8.54	46.49	3.79	5.85
	w/ algorithm	chip	8.82	49	2.51	5.6
		err. (%)	3.3	5.4	34	4.3
	w/o algorithm	chip	7.75	49.4	2.08	4.89
		err. (%)	9.3	6.3	45	16.5

$$\mathbf{\Delta a} = \mathbf{\Delta V} \times \mathbf{S}^{-1} \tag{10}$$

To solve the nonlinear problem, we first approximate concentration $x_i = a_i/\gamma_{i,\text{init}}$, where $\gamma_{i,\text{init}}$ is the activity coefficient of the species i in the reference solution (in this case aCSF). We then calculate the ionic strength, the activity coefficient, and the ionic concentration and iterate this procedure until converging to a reading in the concentration of species in the end solution.

RESULTS AND DISCUSSION

In this study, results obtained with ionic solutions are presented to demonstrate proper operation of the ion-imaging platform. We present the results of sensor training with reference electrode voltage sweep and single-ion runs and lastly validate accurate ion sensing with multi-ion solutions and a brain dialysate fluid sample.

Ion Calibration. The array output for the four ion calibration runs is shown in Figure 3a (top for each ion), where the concentration of each ion is incremented by a decade. The sensor array images for each experiment are included as videos in the Supporting Information. The sensitivity matrix **S** in mV/dec is extracted by averaging all pixel outputs in each ion-selective region and sampling the transient curves of Figure 3a (botton for each ion) at the start and end of the measurement.

$$\mathbf{S} = \begin{bmatrix} S_{K^+K^+} & S_{K^+Na^+} & S_{K^+Ca^{2+}} & S_{K^+H^+} \\ S_{Na^+K^+} & S_{Na^+Na^+} & S_{Na^+Ca^{2+}} & S_{Na^+H^+} \\ S_{Ca^{2+}K^+} & S_{Ca^{2+}Na^+} & S_{Ca^{2+}Ca^{2+}} & S_{Ca^{2+}H^+} \\ S_{H^+K^+} & S_{H^+Na^+} & S_{H^+Ca^{2+}} & S_{H^+H^+} \end{bmatrix} = \begin{bmatrix} 58.9 & 8.15 & -1.48 & -1.33 \\ -0.99 & 53.83 & 1.85 & 2.71 \\ -1.71 & 10.73 & 25.31 & -1.96 \\ 14.8 & 24.3 & 2.14 & 19.2 \end{bmatrix} \tag{11}$$

The matrix demonstrates quasi-Nernstian sensitivity of the K^+-selective membrane to K^+ ions. The Na^+ and Ca^{2+} membranes both achieve near Nernstian performance, taking into account that Ca^{2+} is bivalent. The pH sensitivity is the lowest due to the low purity of the passivation layer. The membrane mapping as derived by the sensor-learning algorithm is shown in Figure 3b alongside the microscope picture of the chip surface to validate the results.

Ion Measurements. To validate the sensing capabilities of the platform and the calibration method, the readout results for the four solutions are summarized in Table 2 and the error is quantified. The conventional readout method (w/o algorithm) is compared with the approach described in this work (w/ algorithm). Following offline training, the results highlight accurate reading of K^+, Na^+, and H^+ ionic concentrations, achieving a maximum error of 11%, while estimations of Ca^{2+} concentration suffer from an average error of 24%. Of course, calcium is bivalent and hence induces a smaller voltage variation for a decade change in concentration; however, the error suggests additional effects arising from the ion-selective membrane/ISFET surface contact. Indeed, the reliable performance shown in Figure S1 (SI) using a PEDOT.PSS solid contact suggests that further optimization is required on the calcium membrane for its adherence to the array. This is acceptable for detection of SDs, which mainly rely on K^+ and Na^+ detection; nevertheless, Ca^{2+} was included to demonstrate opportunities for a wider range of targets.

We hereby demonstrate that the platform is able to perform multi-ion reading and imaging of different ionic solutions. The ISFET array platform is able to reliably discriminate between ions and provide measurements for several targets from a single run.

Brain Dialysate Fluid. To show proof-of-principle of device operation, we now consider human dialysate from a TBI patient. The patient was in the intensive care unit at King's College Hospital and being monitored continuously to determine the metabolic state of the brain. Residual dialysate was collected and frozen for analysis by the device. If the results presented in Table 3 are compared with aCSF perfusate

https://dx.doi.org/10.1021/acs.analchem.9b05836
Anal. Chem. 2020, 92, 5276−5285

Table 3. Results for Ion Readings (mM) and pH

		K^+	(Na^+)	Ca^{2+}	pH
CSF	chip	3.5	(121.8)	1.1	6.02
	spec	3.8	(96.2)	0.99	6.6
	err. (%)	7.7	(26.4)	10.7	9

(Table 2), we see that brain injury has led to an increase in basal K^+ levels together with a decrease in basal Na^+ levels. This is consistent with the injured human brain tissue being partially depolarized, which in turn may explain why such injured tissue is more susceptible to damaging secondary insults such as spreading depolarizations.[10] For completeness, we analyzed the same 20 μL sample using ICP-MS. Very similar results are found with the exception of the Na^+ reading, which was higher on the device. We believe this is an artifact brought about by the low sample volume being unable to completely displace the reference aCSF buffer (with a higher Na^+ concentration of 147 mM) from the Na^+ membrane, which was furthest from the point of injection. To address this limitation, the next generation of the sensing platform is currently being designed with a low volume flow cell for microdialysis.

CONCLUSION

In this paper, we have introduced a potentiometric sensor array platform with sensor-learning algorithms to perform multi-ion imaging, integrated within a LoC architecture able to concurrently sense four electrolytes in a solution. The platform is designed to be versatile, as the CMOS sensors can be covered with polymeric ion-selective membranes to provide selectivity toward electrolytes of interest, which promotes the versatility of the solution to several applications. We have also introduced the notion of sensor learning for a multi-ion ISFET array, based on an offline training clustering algorithm to accommodate the versatility by training the platform to obtain the selectivity and sensitivity of each pixel. The system is demonstrated for several ionic buffer solutions to accurately detect K^+, Na^+, and H^+, while Ca^{2+} has been associated with a larger readout error. As a proof-of-principle, we demonstrate reading with a brain dialysate sample, which allows one to track a change in ionic concentration following spreading depolarization. The platform can be extended to a wider range of species and other applications using the same hardware, but treating the surface with different polymeric coatings, and integrated as part of an end-to-end microfluidic device.

ASSOCIATED CONTENT

Supporting Information

The Supporting Information is available free of charge at https://pubs.acs.org/doi/10.1021/acs.analchem.9b05836.

Figures showing membrane characterization with ISEs, device lifetime, and the learning algorithm, including the reference electrode voltage step, moving average, *k*-means clustering, and DBSCAN, and a caption describing the multi-ion imaging videos (PDF)

Multi-ion imaging videos, including MultiIonImaging_aCSF_Sol4_2x, MultiIonImaging_Calibration_K+_2x, MultiIonImaging_Calibration_Na+_2x, MultiIonImaging_Calibration_Ca+_2x, and MultiIonImaging_Calibration_H+_2x (ZIP)

AUTHOR INFORMATION

Corresponding Authors

Martyn Boutelle − *Department of Bioengineering, Imperial College London, London SW7 2AZ, United Kingdom;* orcid.org/0000-0003-1332-3442; Email: m.boutelle@imperial.ac.uk

Pantelis Georgiou − *Department of Electrical and Electronic Engineering and Institute of Biomedical Engineering, Imperial College London, London SW7 2AZ, United Kingdom;* Email: pantelis@imperial.ac.uk

Authors

Nicolas Moser − *Department of Electrical and Electronic Engineering and Institute of Biomedical Engineering, Imperial College London, London SW7 2AZ, United Kingdom;* orcid.org/0000-0002-6689-0486

Chi Leng Leong − *Department of Bioengineering, Imperial College London, London SW7 2AZ, United Kingdom*

Yuanqi Hu − *Department of Electrical and Electronic Engineering and Institute of Biomedical Engineering, Imperial College London, London SW7 2AZ, United Kingdom*

Chiara Cicatiello − *Department of Electrical and Electronic Engineering and Institute of Biomedical Engineering and Department of Bioengineering, Imperial College London, London SW7 2AZ, United Kingdom*

Sally Gowers − *Department of Bioengineering, Imperial College London, London SW7 2AZ, United Kingdom;* orcid.org/0000-0002-2407-2266

Complete contact information is available at: https://pubs.acs.org/10.1021/acs.analchem.9b05836

Author Contributions

§N.M. and C.L.L. contributed equally to this work as first authors.

Notes

The authors declare no competing financial interest.

ACKNOWLEDGMENTS

This work was supported by the EPSRC Centre for Doctoral Training in High Performance Embedded and Distributed Systems (EP/L016796/1) and the EPSRC Centre for Doctoral Training in Neurotechnology for Life and Health (EP/L016737/1). The dialysate sample was obtained thanks to our collaborators at King's College and the NHS Trust. The spectrometry of the sample was performed by "The Imaging and Analysis Centre, Natural History Museum". The authors would like to acknowledge Hannah Hashem and Theocharis Drakos for providing data on membrane characterization.

REFERENCES

(1) Much, W. E.; Wilcox, C. S. *Am. J. Med.* **1982**, *72*, 536−550.

(2) Reynolds, R. M.; Padfield, P. L.; Seckl, J. R. *British Medical Journal* **2006**, *332*, 702−705.

(3) Strong, A. J.; Fabricius, M.; Boutelle, M. G.; Hibbins, S. J.; Hopwood, S. E.; Jones, R.; Parkin, M. C.; Lauritzen, M. *Stroke* **2002**, *33*, 2738−2743.

(4) Fabricius, M.; Fuhr, S.; Bhatia, R.; Boutelle, M.; Hashemi, P.; Strong, A. J.; Lauritzen, M. *Brain* **2006**, *129*, 778−790.

(5) Dreier, J. P.; Woitzik, J.; Fabricius, M.; Bhatia, R.; Major, S.; Drenckhahn, C.; Lehmann, T. N.; Sarrafzadeh, A.; Willumsen, L.; Hartings, J. A.; Sakowitz, O. W.; Seemann, J. H.; Thieme, A.; Lauritzen, M.; Strong, A. J. *Brain* **2006**, *129*, 3224−3237.

(6) Hartings, J.; et al. *Lancet Neurol.* **2011**, *10*, 1058−1064.

(7) Narayan, R. K.; et al. *J. Neurotrauma* **2002**, *19*, 503−557.
(8) Fabricius, M.; Fuhr, S.; Willumsen, L.; Dreier, J. P.; Bhatia, R.; Boutelle, M. G.; Hartings, J. A.; Bullock, R.; Strong, A. J.; Lauritzen, M. *Clin. Neurophysiol.* **2008**, *119*, 1973−1984.
(9) Leao, A. A. P. *J. Neurophysiol.* **1944**, *7*, 359−390.
(10) Rogers, M. L.; Leong, C. L.; Gowers, S. A.; Samper, I. C.; Jewell, S. L.; Khan, A.; McCarthy, L.; Pahl, C.; Tolias, C. M.; Walsh, D. C.; Strong, A. J.; Boutelle, M. G. *J. Cereb. Blood Flow Metab.* **2017**, *37*, 1883−1895.
(11) Dreier, J. P.; Reiffurth, C.; Woitzik, J.; et al. *Acta Neurochirurgica Supplement* **2015**, *120*, 137−140.
(12) Mayr, T.; Liebsch, G.; Klimant, I.; Wolfbeis, O. S. *Analyst* **2002**, *127*, 201−203.
(13) Ueyama, H.; Takagi, M.; Takenaka, S. *J. Am. Chem. Soc.* **2002**, *124*, 14286−14287.
(14) Hisamoto, H.; Yasuoka, M.; Terabe, S. *Anal. Chim. Acta* **2006**, *556*, 164−170.
(15) Wang, L.; Sadler, S.; Cao, T.; Xie, X.; Von Filseck, J. M.; Bakker, E. *Anal. Chem.* **2019**, *91*, 8973−8978.
(16) Yoshinobu, T.; Iwasaki, H.; Ui, Y.; Furuichi, K.; Ermolenko, Y.; Mourzina, Y.; Wagner, T.; Näther, N.; Schöning, M. *Methods* **2005**, *37*, 94−102.
(17) Miyamoto, K.; Kuwabara, Y.; Kanoh, S.; Yoshinobu, T.; Wagner, T.; Schöning, M. J. *Sens. Actuators, B* **2009**, *137*, 533−538.
(18) Miyamoto, K.-i.; Itabashi, A.; Wagner, T.; Schöning, M. J.; Yoshinobu, T. *Sens. Actuators, B* **2014**, *194*, 521−527.
(19) Fossum, E. R. *IEEE Trans. Electron Devices* **1997**, *44*, 1689−1698.
(20) Lichtsteiner, P.; Posch, C.; Delbruck, T. *IEEE J. Solid-State Circuits* **2008**, *43*, 566−576.
(21) Mendis, S. K.; Kemeny, S. E.; Gee, R. C.; Pain, B.; Staller, C. O.; Kim, Q.; Fossum, E. R. *IEEE J. Solid-State Circuits* **1997**, *32*, 187−197.
(22) Abbott, J.; Ye, T.; Krenek, K.; Gertner, R. S.; Ban, S.; Kim, Y.; Qin, L.; Wu, W.; Park, H.; Ham, D. *Nat. Biomed. Eng.* **2020**, *4*, 232.
(23) Tedjo, W.; Nejad, J. E.; Feeny, R.; Yang, L.; Henry, C. S.; Tobet, S.; Chen, T. *Biosens. Bioelectron.* **2018**, *114*, 78−88.
(24) Hattori, T.; Tamamura, Y.; Tokunaga, K.; Sakurai, T.; Kato, R.; Sawada, K. *Anal. Chem.* **2014**, *86*, 4196−4201.
(25) Hattori, T.; Satou, H.; Tokunaga, K.; Kato, R.; Sawada, K. *Sens. Mater.* **2015**, *27*, 1023−1034.
(26) Futagawa, M.; Suzuki, D.; Otake, R.; Dasai, F.; Ishida, M.; Sawada, K. *IEEE Trans. Electron Devices* **2013**, *60*, 2634−2639.
(27) Bergveld, P. *Sens. Actuators, B* **2003**, *88*, 1−12.
(28) Moser, N.; Lande, T. S.; Toumazou, C.; Georgiou, P. *IEEE Sens. J.* **2016**, *16*, 6496−6514.
(29) Bausells, J.; Carrabina, J.; Errachid, A.; Merlos, A. *Sens. Actuators, B* **1999**, *57*, 56−62.
(30) Hu, Y.; Moser, N.; Georgiou, P. *IEEE Sens. J.* **2017**, *17*, 5276−5284.
(31) Moser, N.; Rodriguez-Manzano, J.; Lande, T. S.; Georgiou, P. *IEEE Transactions on Biomedical Circuits and Systems* **2018**, *12*, 390−401.
(32) Shields, P.; Nemeth, B.; Green, R.; Riehle, M.; Cumming, D. *IEEE Sens. J.* **2012**, *12*, 2744−2749.
(33) Rothberg, J. M.; et al. *Nature* **2011**, *475*, 348−352.
(34) Moser, N.; Rodriguez-Manzano, J.; Yu, L. S.; Kalofonou, M.; de Mateo, S.; Li, X.; Lande, T. S.; Toumazou, C.; Georgiou, P. Live demonstration: A CMOS-based ISFET array for rapid diagnosis of the Zika virus. *2017 IEEE International Symposium on Circuits and Systems (ISCAS)*; IEEE, 2017; pp 1−1.
(35) Walsh, K. B.; DeRoller, N.; Zhu, Y.; Koley, G. *Biosens. Bioelectron.* **2014**, *54*, 448−454.
(36) Mizutani, S.; Takahashi, S.; Kono, A.; Hattori, T.; Iwata, T.; Ishida, M.; Sawada, K. Development of amperometric ion sensor array for multi-ion detection. *2015 IEEE Sensors*; IEEE, 2015; pp 1−4.
(37) Moser, N.; Leng Leong, C.; Hu, Y.; Boutelle, M.; Georgiou, P. An Ion Imaging ISFET Array for Potassium and Sodium Detection. *2016 IEEE International Symposium on Circuits and Systems (ISCAS)*; IEEE, 2016.
(38) Duarte-Guevara, C.; Lai, F.-L.; Cheng, C.-W.; Reddy, B.; Salm, E.; Swaminathan, V.; Tsui, Y.-K.; Tuan, H. C.; Kalnitsky, A.; Liu, Y.-S.; Bashir, R. *Anal. Chem.* **2014**, *86*, 8359−8367.
(39) Mikolajick, T.; Kühnhold, R.; Ryssel, H. *Sens. Actuators, B* **1997**, *44*, 262−267.
(40) Georgiou, P.; Toumazou, C. *Sens. Actuators, B* **2009**, *143*, 211−217.
(41) Chan, D.; Healy, T. W.; White, L. R. *J. Chem. Soc., Faraday Trans. 1* **1976**, *72*, 2844−2865.
(42) Bousse, L.; De Rooij, N.; Bergveld, P. *IEEE Trans. Electron Devices* **1983**, *30*, 1263−1270.
(43) Shepherd, L.; Toumazou, C. *Circuits and Systems I: Regular Papers, IEEE Transactions on* **2005**, *52*, 2614−2619.
(44) Hu, Y.; Georgiou, P. *IEEE Trans. Biomed. Circuits Syst.* **2014**, *8*, 177−185.
(45) Band, D. M.; Kratochvil, J.; Wilson, P. A.; Treasure, T. *Analyst* **1978**, *103*, 246−251.
(46) Bakker, E.; Pretsch, E. *TrAC, Trends Anal. Chem.* **2005**, *24*, 199−207.
(47) Fibbioli, M.; Morf, W. E.; Badertscher, M.; De Rooij, N. F.; Pretsch, E. *Electroanalysis* **2000**, *12*, 1286−1292.
(48) Papp, S.; Bojtár, M.; Gyurcsányi, R. E.; Lindfors, T. *Anal. Chem.* **2019**, *91*, 9111−9118.

https://dx.doi.org/10.1021/acs.analchem.9b05836
Anal. Chem. 2020, 92, 5276−5285